A 3-D Scattering Model for Orientation-dependent X-ray Dark-field Imaging

Shiyang Hu*†, Andreas Maier*, Joachim Hornegger*, Florian Bayer§, Thomas Weber§
Gisela Anton§ and Christian Riess*‡
*Pattern Recognition Lab, Department of Computer Science
Friedrich-Alexander University of Erlangen-Nuremberg, Erlangen, Germany,
†Erlangen Graduate School in Advanced Optical Technologies (SAOT)
Friedrich-Alexander University of Erlangen-Nuremberg, Erlangen, Germany
‡Department of Radiology, Stanford University, Palo Alto, California, USA
§Erlangen Centre for Astroparticle Physics (ECAP)
Friedrich-Alexander University of Erlangen-Nuremberg, Erlangen, Germany

***Abstract*—X-ray dark-field imaging has drawn attention in recent years for its great diagnostic potential. This novel modality measures structural variations at length scales of few hundred nanometers using a conventional X-ray tube. It yields high contrast to some structures composed of weakly absorbing materials. The dark-field signals are generated by orientations of the micro structures in the objects and thus enable reconstruction of local 3-D orientations.**

The main barrier for fully recovering the 3-D micro structure orientation is that, to our knowledge, currently no analytic linear projection formula exists. In this paper, we develop a 3-D X-ray dark-field scattering model. This model is experimentally validated by dark-field images of bunches of fibers. This is a major step towards the inversion of the orientation-dependent dark-field line integral. Based on this model, fully vectorial dark-field reconstruction can be expected in future.

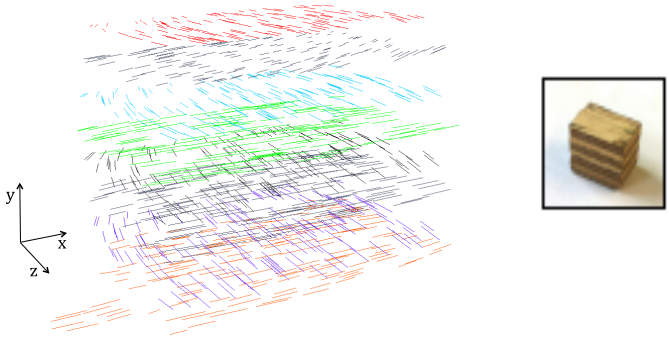

Fig. 1. Wooden block (right), consisting of multiple layers of spliced wood in different orientations. 2-D reconstruction (left) of the wooden block. Color coding is used to distinguish different layers.

I. Introduction

The X-ray dark-field signal shows microscopic inhomogeneities in specimen. Currently, Talbot-Lau interferometers are the most popular systems to capture dark-field images using a conventional X-ray tube [1], [2]. The potential of this novel modality is twofold:

1) it allows recovery of local orientations of micro structures [3], and
2) it allows reconstruction of the structural variations at length scales below the resolution of conventional X-ray imaging systems [4].

Previous works have partially reconstructed local orientations. However, the reconstructed orientations are based on inadequate projection models that limit the reconstruction. Revol *et al.* [3] assume that the orientations are available as prior knowledge. The algorithm by Malecki *et al.* [5] requires to collect rays from all three axes of rotation, and hence requires a considerably larger number of X-ray images. In our previous work [4], the projection model is based on 2-D structural information, thus only in-plane orientations are reconstructed. 3-D reconstruction is possible, but micro structure orientations can only be recovered within the plane of scan rotation as shown in Fig 1. The vectorial information with the missing dimension can be obtained using projections from two tomographic trajectories [6]. However, this approach requires at least two tomographic scans on different trajectories, which is challenging to implement in an actual system.

In this paper, we propose a projection model where the 3-D orientations of micro structures are described as elevation and azimuth angles. We assume that an elongated micro structure exhibits a 3-D Gaussian scattering distribution. X-ray dark-field signals of fibers located at different elevation angles are analyzed according to the proposed model.

II. 3-D Scattering Model

In our model, scattering from a single elongated structure is modeled as a Gaussian distribution. Statistically, this approximation exploits the idea that the scattering function of an elongated structure can be derived as convolution of scattering functions of individual scatterers and thus obeys the central limit theorem to form a Gaussian distribution [7]. Previous works experimentally validated this idea for a 2-D Gaussian approximation for in-plane scattering [7], [8]. In this paper, we perform the extension to 3-D and experimentally validate the proposed model. In this section, we first model local

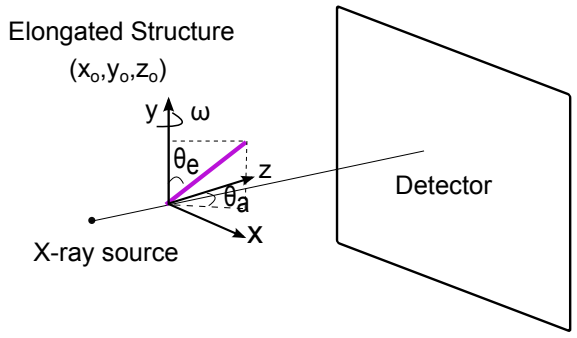

Fig. 2. Geometry and coordinate systems

micro structure orientations in the global imaging coordinate system. Then, we use this formulation to derive dark-field contrast using an analytic representation of a grating-based X-ray phase-contrast system.

A. 3-D Gaussian Scattering Distribution in Imaging Coordinates

Let $\boldsymbol{p} = (x, y, z)^{\mathrm{T}}$ denote a point in the imaging coordinate system, and let $\boldsymbol{p}_o = (x_o, y_o, z_o)^{\mathrm{T}}$ denote a point in the coordinate system of the local structure. Let furthermore θ_e and θ_a denote the elevation and azimuth angle of an elongated structure in the imaging coordinate system, as shown in Fig. 2. A 3-D Gaussian function $f_g(\boldsymbol{p}_o)$ with zero mean and diagonal covariance matrix $\Sigma = \mathrm{diag}(\delta_1, \delta_2, \delta_3)$ (which is determined by the material of the sample) can be written as

$$f_g(\boldsymbol{p}_o) = \frac{1}{(2\pi)^{\frac{3}{2}}\delta_1\delta_2\delta_3} \exp\left(-\frac{1}{2\delta_1^2}x_o^2 - \frac{1}{2\delta_2^2}y_o^2 - \frac{1}{2\delta_3^2}z_o^2\right) \quad . \tag{1}$$

Note that throughout the paper, we omit for all components of the covariance matrices the dependency on the location $\boldsymbol{p}_o$ or $\boldsymbol{p}$, respectively.

Imaging coordinates can be transformed into structure coordinates using two rotation matrices for elevation and azimuth angle. This yields the relation

$$\boldsymbol{p}_o = R \cdot \boldsymbol{p} \ , \tag{2}$$

where

$$\begin{aligned} R &= \begin{bmatrix} \sin\theta_e & -\cos\theta_e & 0 \\ \cos\theta_e & \sin\theta_e & 0 \\ 0 & 0 & 1 \end{bmatrix} \begin{bmatrix} \sin\theta_a & 0 & -\cos\theta_a \\ 0 & 1 & 0 \\ \cos\theta_a & 0 & \sin\theta_a \end{bmatrix} \\ &= \begin{bmatrix} \sin\theta_e\sin\theta_a & -\cos\theta_e & -\sin\theta_e\cos\theta_a \\ \cos\theta_e\sin\theta_a & \sin\theta_e & -\cos\theta_a\cos\theta_e \\ \cos\theta_a & 0 & \sin\theta_a \end{bmatrix} \quad . \end{aligned} \tag{3}$$

Note that we ignore the roll angle in this formulation, as different tomographic views do not affect it. Instead, we assume that the roll angle is implicitly modeled in the covariance matrix Σ.

All local micro structure orientations can be expressed in global coordinates by substituting Eq. 3 into Eq. 1. We define the resulting function as $s(\boldsymbol{p})$,

$$\begin{aligned} s(\boldsymbol{p}) = &\frac{1}{(2\pi)^{\frac{3}{2}}\delta_1\delta_2\delta_3} \exp(-(a_1x^2 + 2a_2xy \\ &+ a_3y^2 + 2a_4yz + a_5z^2 + 2a_6xz)) \ . \end{aligned} \tag{4}$$

Here,

$$\begin{aligned} a_1 =& \frac{\sin^2\theta_e\sin^2\theta_a}{2\delta_1^2} + \frac{\cos^2\theta_e\sin^2\theta_a}{2\delta_2^2} + \frac{\cos^2\theta_a}{2\delta_3^2} \\ a_2 =& \cos\theta_e\sin\theta_e\sin\theta_a\left(-\frac{1}{2\delta_1^2} + \frac{1}{2\delta_2^2}\right) \\ a_3 =& \frac{\cos^2\theta_e}{2\delta_1^2} + \frac{\sin^2\theta_e}{2\delta_2^2} \\ a_4 =& \cos\theta_e\sin\theta_e\cos\theta_a\left(\frac{1}{2\delta_1^2} - \frac{1}{2\delta_2^2}\right) \\ a_5 =& \frac{\sin^2\theta_e\cos^2\theta_a}{2\delta_1^2} + \frac{\cos^2\theta_e\cos^2\theta_a}{2\delta_2^2} + \frac{\sin^2\theta_a}{2\delta_3^2} \\ a_6 =& \sin\theta_a\cos\theta_a\left(-\frac{\sin^2\theta_e}{2\delta_1^2} - \frac{\cos^2\theta_e}{2\delta_2^2}\right) \\ &+ \frac{\cos\theta_a\sin\theta_a}{2\delta_3^2} \end{aligned} \tag{5}$$

We consider a parallel-beam imaging system. Then, after rotation by angle ω, the elongated structure's elevation angle is θ_e and the azimuth angle is $\theta_a - \omega$.

B. Dark-field scatter in a Talbot-Lau Interferometer

Equation 4 can be further simplified by taking the particularities of a Talbot-Lau interferometer into account. Here, dark-field signals are only measured perpendicularly to the grating bars and X-ray propagation direction, i.e., only scattering projected to x-axis in Fig. 2 is measured by dark-field imaging. Integrating the above scattering function along both y-axis and z-axis results in

$$s(x) = \frac{1}{\sqrt{2\pi\delta}} \exp\left(\frac{-x^2}{2\delta^2}\right) \ , \tag{6}$$

$$\begin{aligned} \delta^2 =& (\delta_1^2 + (\delta_2^2 - \delta_1^2)\cos^2\theta_e) \\ &+ ((\delta_3^2 - \delta_1^2) + (\delta_1^2 - \delta_2^2)\cos^2\theta_e)\cos^2(\theta_a - \omega) \end{aligned} \tag{7}$$

Previous work described that intensity can be well approximated by first-order Fourier expansion [1],

$$I^r(\boldsymbol{p}_d, \omega) \approx a_0(\boldsymbol{p}_d, \omega) + a_1(\boldsymbol{p}_d, \omega)\cos\left(\frac{2\pi}{g_2}x_g - \Phi(\boldsymbol{p}_d, \omega)\right) \tag{8}$$

where $\boldsymbol{p}_d$ denotes the pixel position on the detector, x_g is the position of grating with period g_2, ω is the rotation angle of the scanned object around the y-axis. $a_0(\boldsymbol{p}_d, \omega), a_1(\boldsymbol{p}_d, \omega)$ are offset and amplitude of the oscillating intensity signal. $\Phi(\boldsymbol{p}_d, \omega)$ denotes the lateral phase shift. The observed intensity $I^s(\boldsymbol{p}_d, \omega)$ (after the X-ray passing through the object) can be

calculated as the convolution of the original intensity $I^r(\boldsymbol{p}_d, \omega)$ with the scattering function $s(x)$ as

$$\begin{aligned} I^s(\boldsymbol{p}_d, \omega) &= I^r(\boldsymbol{p}_d, \omega) * s(x) \\ &= a_0 + a_1 \exp\left(\frac{-2\pi\delta^2}{g_2^2}\right) \cos\left(\frac{2\pi}{g_2} x_g - \Phi(i,j)\right) \quad . \end{aligned} \tag{9}$$

The dark-field signal is defined as visibility contrast

$$d(\boldsymbol{p}_d, \omega) = \frac{a_1^s(\boldsymbol{p}_d, \omega)/a_0^s(\boldsymbol{p}_d, \omega)}{a_1^r(\boldsymbol{p}_d, \omega)/a_0^r(\boldsymbol{p}_d, \omega)} \quad , \tag{10}$$

where a_0^s and a_1^s denote captured images with the object in place (cf. Eq. 8), and a_0^r, a_1^r denote captured images of an empty scene (cf. Eq. 9). Hence,

$$d(\boldsymbol{p}_d, \omega) = \exp\left(\frac{-2\pi\delta^2}{g_2^2}\right) \quad . \tag{11}$$

Substituting Eq. 7 into Eq. 11, we obtain

$$\begin{aligned} &d(\boldsymbol{p}_d, \omega) = \\ &\exp\left(-(b_1 + b_2\cos^2\theta_e) - (b_3 - b_2\cos^2\theta_e)\cos^2(\theta_a - \omega)\right) \end{aligned} \tag{12}$$

where

$$\begin{aligned} b_1 &= \frac{2\pi}{g_2^2} \cdot \delta_1^2 \quad , \\ b_2 &= \frac{2\pi}{g_2^2} \cdot (\delta_1^2 - \delta_2^2) \quad , \\ b_3 &= \frac{2\pi}{g_2^2} \cdot (\delta_3^2 - \delta_1^2) \quad . \end{aligned} \tag{13}$$

Taking the negative logarithm of $d(\boldsymbol{x}, \omega)$, the log-dark-field of an elongated structure is

$$\begin{aligned} &d_{\log}(\boldsymbol{p}_d, \omega) = -\log(D(\boldsymbol{p}_d, \omega)) \\ &= (b_1 + b_2\cos^2\theta_e) + (b_3 - b_2\cos^2\theta_e)\cos^2(\theta_a - \omega) \end{aligned} \quad . \tag{14}$$

III. Experiments and Results

To evaluate our proposed projection model, we examined dark-field images of carbon fiber bunch at elevation angles $30°, 45°$ and $60°$. A thin glass capillary filled with carbon fiber was scanned over $720°$ at azimuthal steps of $18°$, i.e., 40 projections per scan. Example dark-field images are shown in Fig.3. For each elevation angle, images are shown at azimuth angles of $0°, 36°, 90°$, respectively. One can observe the impact of azimuth angle and elevation angle on the dark-field signals.

We calculated b_1, b_2 and b_3 using log-dark-filed acquired at elevation angles of $30°$ and $60°$. For each data set, we averaged the log-dark-field over a region of interest in each projection (i.e. the region only contains log-dark-field of carbon fibers, not glass capillary). Line fitting was applied to calculate coefficients depending on different elevation angles. In Fig. 4, the fitted line is presented. The blue stars are the processed

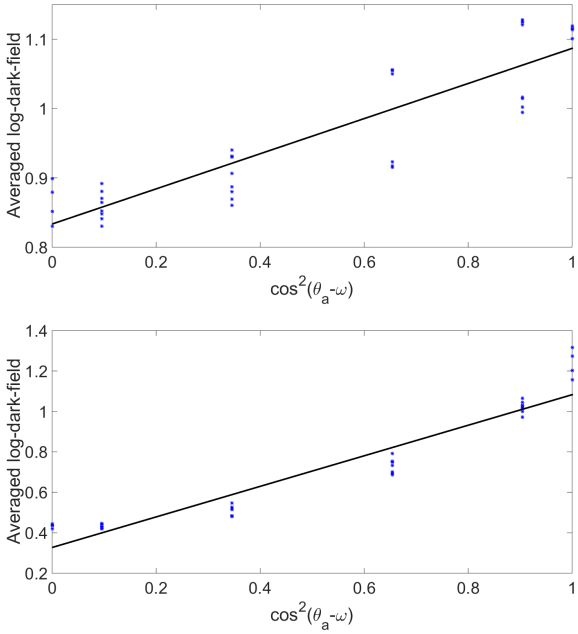

Fig. 4. Line fitting of averaged log-dark-field contributions over region of interest at elevation angle: a) $30°$, b) $60°$. Blue starts denote the data points and the black lines are the fitted lines. Normalized least square root error (NLSRE) for the two dataset are: a) NLSRE=5.0%; b) NLSRE=3.8%

data fitted by the green line. To evaluate our result, we use the normalized least square root error (NLSRE):

$$r = \frac{\sqrt{\sum_{i=1}^{N_p} (\bar{d}_a(i) - \bar{d}_s(i))^2}}{N_p \cdot \left(\max\limits_{i=1\ldots N_p} \bar{d}_a(i) - \min\limits_{i=1\ldots N_p} \bar{d}_a(i)\right)} \quad , \tag{15}$$

where $N_p = 40$ is the number of projections, $d_a(i)$ is the averaged log-dark-field at ith projection and $d_s(i)$ is the line fitting value at ith projection. For elevation angle $30°$, the NLSRE is 5.0% and the NLSRE for elevation angle $60°$ is 3.8%.

From two sets of coefficients, b_1, b_2 and b_3 can be calculated. In our experiment, the results are: $b_1 = 0.074, b_2 = 1.008, b_3 = 1.006$. In Fig. 5, we show the simulation log-dark-field of a single carbon fiber bunch at elevation angle $45°$ based on the proposed scattering model (red line). These results are compared with experimental acquisition (averaged log-dark-field contributions over region of interest) denoted by the blue line. The figure shows high agreement between the prediction and actual measurements in an experimental setup. Similar to NLSRE, we define normalized square root difference (NSRD) for a quantitative evaluation:

$$r_d = \frac{\sqrt{\sum_{i=1}^{N_p} (d_{\log}^e(i) - d_{\log}^s(i))^2}}{N_p \cdot \left(\max\limits_{i=1\ldots N_p} d_{\log}^e(i) - \min\limits_{i=1\ldots N_p} d_{\log}^e(i)\right)} \tag{16}$$

where $N_p = 40$ is the number of projections, $d_{\log}^e(i), d_{\log}^s(i)$

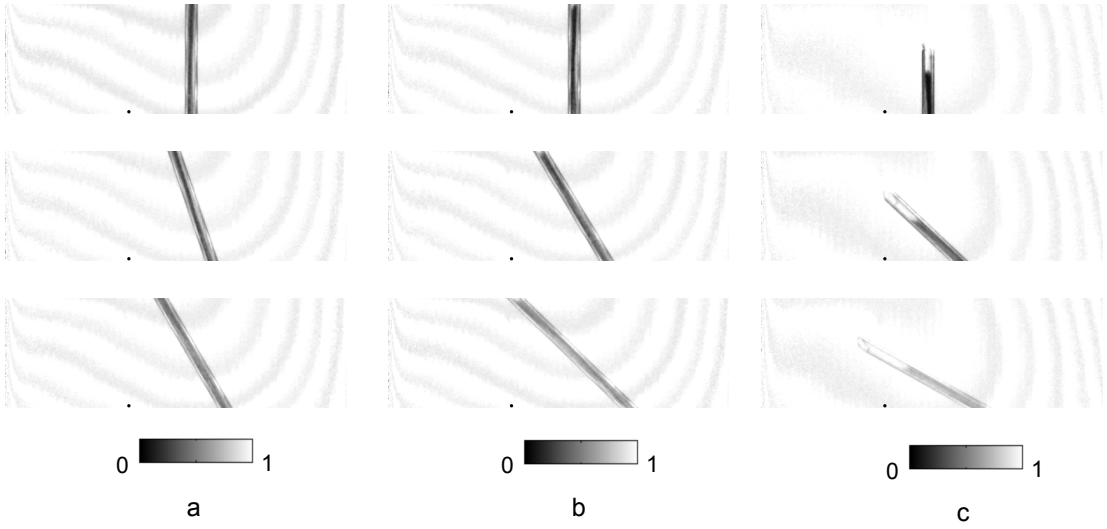

Fig. 3. Dark-field images of a single carbon fiber bunch for elevation angle: a) $30°$, b) $45°$ and c) $60°$. Each column shows a series of three dark-field images obtained at azimuth angle $0°, 36°, 90°$.

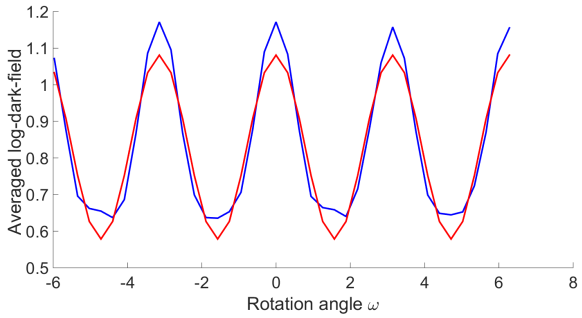

Fig. 5. Comparison of simulated average log-dark-field of the carbon bunch at elevation angle $45°$ (red line) and the experimental dark-field signals of the same example (blue line).

are the averaged log-dark-field from experiments and simulation at ith projection. The resulted NSRD is 1.1%.

IV. Discussion and Conclusion

In this paper, we propose a 3-D scattering model derived from a 3-D Gaussian distribution. We examine and evaluate this formulation by comparing simulated signals and experimental results. Our experimental results show excellent agreement with the model prediction. We consider this a major step towards reconstruction of the local micro structure orientation fully three-dimensionally. We expect that a line integral model can be formed from this observation as a voxel-wise sum of overlaying scattering structures as reported in the literature for the 2-D case [4]. With such a model, it is possible to tackle the inverse problem of reconstruction of 3-D micro structure orientations.

Acknowledgment

The authors acknowledge funding of the Erlangen Graduate School in Advanced Optical Technologies (SAOT) by the German Research Foundation (DFG) in the framework of the German excellence initiative. Furthermore, we acknowledge support from the RTG 1773 by the German Research Foundation.

References

[1] F. Pfeiffer, M. Bech, O. Bunk, P. Kraft, E. F. Eikenberry, C. Brönnimann, C. Grünzweig, and C. David, "Hard-x-ray dark-field imaging using a grating interferometer," *Nature materials*, vol. 7, no. 2, pp. 134–137, 2008.

[2] S. Kaeppler, F. Bayer, T. Weber, A. Maier, G. Anton, J. Hornegger, M. Beckmann, P. A. Fasching, A. Hartmann, F. Heindl *et al.*, "Signal decomposition for x-ray dark-field imaging," in *Medical Image Computing and Computer-Assisted Intervention–MICCAI 2014*. Springer, 2014, pp. 170–177.

[3] V. Revol, C. Kottler, R. Kaufmann, A. Neels, and A. Dommann, "Orientation-selective X-ray dark field imaging of ordered systems," *Journal of Applied Physics*, vol. 112, no. 11, p. 114903, 2012. [Online]. Available: http://link.aip.org/link/JAPIAU/v112/i11/p114903/s1&Agg=doi

[4] F. L. Bayer, S. Hu, A. Maier, T. Weber, G. Anton, T. Michel, and C. P. Riess, "Reconstruction of scalar and vectorial components in x-ray dark-field tomography," *Proceedings of the National Academy of Sciences*, vol. 111, no. 35, pp. 12 699–12 704, 2014.

[5] A. Malecki, G. Potdevin, T. Biernath, E. Eggl, K. Willer, T. Lasser, J. Maisenbacher, J. Gibmeier, A. Wanner, and F. Pfeiffer, "X-ray tensor tomography," *EPL (Europhysics Letters)*, vol. 105, no. 3, p. 38002, 2014.

[6] S. Hu, C. Riess, J. Hornegger, P. Fischer, F. Bayer, T. Weber, G. Anton, and A. Maier, "3-d tensor reconstruction in x-ray dark-field tomography," in *Bildverarbeitung für die Medizin 2015*. Springer, 2015, pp. 492–497.

[7] G. Khelashvili, J. G. Brankov, D. Chapman, M. A. Anastasio, Y. Yang, Z. Zhong, and M. N. Wernick, "A physical model of multiple-image radiography," *Physics in medicine and biology*, vol. 51, no. 2, p. 221, 2006.

[8] T. H. Jensen, M. Bech, I. Zanette, T. Weitkamp, C. David, H. Deyhle, S. Rutishauser, E. Reznikova, J. Mohr, R. Feidenhans *et al.*, "Directional x-ray dark-field imaging of strongly ordered systems," *Physical Review B*, vol. 82, no. 21, p. 214103, 2010.